International Journal of Thermal Sciences 204 (2024) 109219

Contents lists available at ScienceDirect

International Journal of Thermal Sciences

journal homepage: www.elsevier.com/locate/ijts

Comprehensive comparative study of experimental and simulated critical heat flux in special high-flux cooling devices: The Short Helical Minichannel-Evaporators

M. Feiner [a], F.J. Fernández [b,*], M. Arnemann [a], M. Kipfmüller [a]

[a] University of Applied Sciences, Moltkestr. 30, 76131 Karlsruhe, Germany
[b] University of Oviedo, Polytechnic School of Engineering, C/Wifredo Ricart, 33204 Gijón, Spain

ARTICLE INFO

Keywords:
Critical heat flux
High flux heat removal
Short helical minichannel evaporator
Groeneveld model
Performance optimization
Experimental benchmarking

ABSTRACT

Short Helical Minichannel Evaporators are compact heat exchangers characterized by small, helical channels that allow high heat flux dissipation by means of direct cooling. It is a promising cooling solution in applications requiring high heat transfer rates in a limited space, such as power electronics, machining processes, injection molding among others. Optimal and safe operation of these devices is critically dependent on accurate determination of the critical heat flux (CHF) when nucleate boiling changes to filmwise regime. Misestimation of the CHF could lead to system burnout or suboptimal performance, highlighting the need for reliable theoretical models. In this study, the performance of a theoretical model was compared with a series of experiments carried out on a custom-built test rig. The results show a strong correlation between the experimental data and the adapted Groeneveld model, with a Mean Absolute Error (MAE) of $8.51\,\mathrm{kW\,m^{-2}}$, a Mean Error (ME) of $-4.71\,\mathrm{kW\,m^{-2}}$, and a Deviation (Dev) of $8.77\,\mathrm{kW\,m^{-2}}$. Notably, 96.8% of the simulated values were within a 15% error band. The validated model is also applied to increase knowledge about design parameters beyond the experimental data. The study emphasizes the practicality of the Groeneveld model in accurately calculating the CHF for these specific heat exchangers, encouraging improvements for performance and operational safety.

1. Introduction

The rapid technological advancements and the trend towards miniaturization have significantly heightened the demand for efficient, compact thermal management systems. Short Helical Minichannel Evaporators (SHMEs) are special cooling devices that can be a key solution in this context, offering exceptional heat transfer capabilities and a compact form factor. They are particularly beneficial for high heat flux applications in constrained spaces, such as in power electronics, battery cooling, and various manufacturing processes.

In power electronics, the miniaturization trend has resulted in increased power densities, necessitating efficient and space-saving cooling solutions. SHMEs excel in this role, offering high heat transfer rates within a limited volume. This makes them integral in maintaining optimal operating temperatures, thus enhancing the performance and reliability of electronic devices. Their compact design and efficiency make SHMEs ideal for battery systems and in manufacturing processes where precise temperature control is essential.

The importance of SHMEs in thermal management is growing, driven by their application in diverse high-tech fields. They are expected to play a crucial role in providing effective cooling solutions to meet the evolving demands of modern technology.

In the field of injection molding, where rapid cooling cycles are crucial for productivity, SHMEs can play an important role. By operating closer to the CHF limit without exceeding it, SHMEs can extract heat from the mold cavity more effectively, significantly reducing cooling times. This translates to quicker production cycles, boosting overall productivity in the manufacturing process.

Traditional methods for sonotrode cooling, often relying on water baths, can disrupt production with necessary interruptions for refilling or temperature control. SHMEs offer a promising alternative for internal sonotrode cooling. By implementing SHMEs directly within the sonotrode design, continuous operation becomes achievable. The SHMEs provide efficient heat removal directly from the sonotrode itself, eliminating the need for external cooling baths and their associated

* Corresponding author.
E-mail addresses: matthias.feiner@gmx.de (M. Feiner), javierfernandez@uniovi.es (F.J. Fernández), michael.arnemann@h-ka.de (M. Arnemann), martin.kipfmueller@h-ka.de (M. Kipfmüller).

https://doi.org/10.1016/j.ijthermalsci.2024.109219
Received 15 February 2024; Received in revised form 23 May 2024; Accepted 13 June 2024
Available online 21 June 2024

Nomenclature

Abbreviations

CHF	Critical Heat Flux
Dev	Deviation
MAE	Mean Absolute Error
ME	Mean Error
SHME	Short helical minichannel evaporator

Symbols

$\dot{m}$	mass flow rate in $\frac{\mathrm{kg}}{\mathrm{s}}$
$\dot{Q}$	Heat power in W
$\dot{q}$	Heat flux in $\frac{\mathrm{W}}{\mathrm{m}^2}$
A	Area in mm^2
D	Bore diameter in mm
d_{hyd}	Hydraulic diameter in mm
G	mass flux in $\frac{\mathrm{kg}}{\mathrm{s\,m}^2}$
h	Specific enthalpy in $\frac{\mathrm{J}}{\mathrm{kg}}$
L	Evaporator length in mm
P	Pitch in mm
p	Pressure in Pa
r	Mean radius in mm
S	Engagement length in mm
T	Temperature in °C
U	Perimeter in mm
x	vapor quality
z	Bore length in mm

Subscripts

c	Condensation
crit	Critical
el	Electrical
in	At inlet conditions
l	Refering to the liquid phase
max	Maximum
mea	Measured
o	Evaporation
out	At outlet conditions
sat	Saturation
sim	Simulated
swirl	Refering to swirl flow
w	At the wall

interruptions. This continuous cooling capability translates to uninterrupted sonotrode operation, streamlining production processes and potentially enhancing overall throughput.

Understanding Critical Heat Flux (CHF) is essential in the design and operation of evaporative heat exchangers, particularly in the context of SHMEs. CHF represents the maximum heat transfer limit by convective boiling, marking the transition from nucleate to film boiling on the heat exchanger wall. Although studies like Nukiyama's have explored systems with distinct heating surface temperatures, practical applications more commonly involve systems with distinct heat fluxes. Exceeding the CHF point can lead to a rapid increase in wall temperature, risking the collapse of the cooling process and potential damage to the heating surface. This phenomenon applies to refrigerants as well as water [1–4].

This study investigates CHF as a key design parameter in a novel geometry designed for high heat flux cooling. Existing research in CHF has primarily focused on straight microchannels or larger helical geometries with much longer evaporator sections. This work explores the unique influence of the helical design on CHF in these short minichannels. A combined approach is employed, utilizing both experimental data and a validated, adapted model. This not only provides valuable data for CHF prediction but also offers deeper insights into the underlying physical mechanisms.

Table 1
Steps in the cycle process.

Step	Process
0→1	Fitting to the capillary tube (sudden cross-section narrowing)
1→2	Liquid single phase pressure loss in the capillary tube
2→3	Two-phase pressure drop in the capillary tube
3→4	At the capillary outlet, the refrigerant expands as a spray channel onto the end face of the pocket hole
4→5	The refrigerant counterflow enters the helical geometry against the inflow direction and continues to evaporate with additional pressure drop. This area is also called the swirl part of the evaporator
5→6	If the heat input is high enough, the refrigerant will already overheat in this area
6→7	For compressor safety additional post evaporator assures overheating of the refrigerant
7→8	The refrigerant is compressed to condensation pressure
8→0	Refrigerant condensation in the condenser and subcooling in an additional heat exchanger

Numerous factors influence CHF in flow boiling, including flow pattern, type of flow, condition of the heat transfer surface, type of heating, and thermodynamic properties, as well as the geometry of the cooling channel [5]. Traditionally associated with high heat flux management in power plant applications, the significance of CHF has expanded into power electronics with higher power densities than traditional power plants. This shift underscores the increasing relevance of CHF in contemporary applications [5].

The SHME represents a significant development in thermal management. With a unique design resembling a helical screw and an evaporator channel diameter typically between 0.85 and 1.85 mm, SHME combines compact size with efficient heat dissipation [6,7]. This design effectively bridges the gap between traditional high heat flux applications and the escalating challenges in high-density power electronics.

However, the field lacks comprehensive literature focusing specifically on SHMEs, particularly regarding heat transfer phenomena in small diameter helical evaporator geometries [8–11]. There is a pressing need to explore these types of evaporators further and elucidate the complex processes involved.

The SHME design in the refrigeration circuit is shown schematically in Fig. 1. The refrigerant is introduced via a capillary into a component, deflecting it 180° at the bottom of the hole and forcing it to exit in a helical pattern, which improves heat transfer and increases CHF. The design cools both front and side surfaces of a blind hole, with refrigerant injected through a capillary and expelled in the opposite direction to the injection.

Fig. 2 shows a pressure-enthalpy diagram explaining the evaporator processes (detailed in Table 1). After a pressure drop in the fitting and capillary (due to geometry and friction), the refrigerant may become two-phase depending on flow conditions. It then sprays against the hot face, evaporating partially and swirling within the helical channel (shown in bold on Fig. 2). Standard refrigeration cycle steps outside the evaporator are shown with the thin black line.

The SHME's simplistic manufacturability, high heat flux handling, and precision in heat dissipation make it suitable for a wide range of applications, from cooling in plastic injection molding and linear motors to machining processes of nickel-based alloys like Inconel 718.

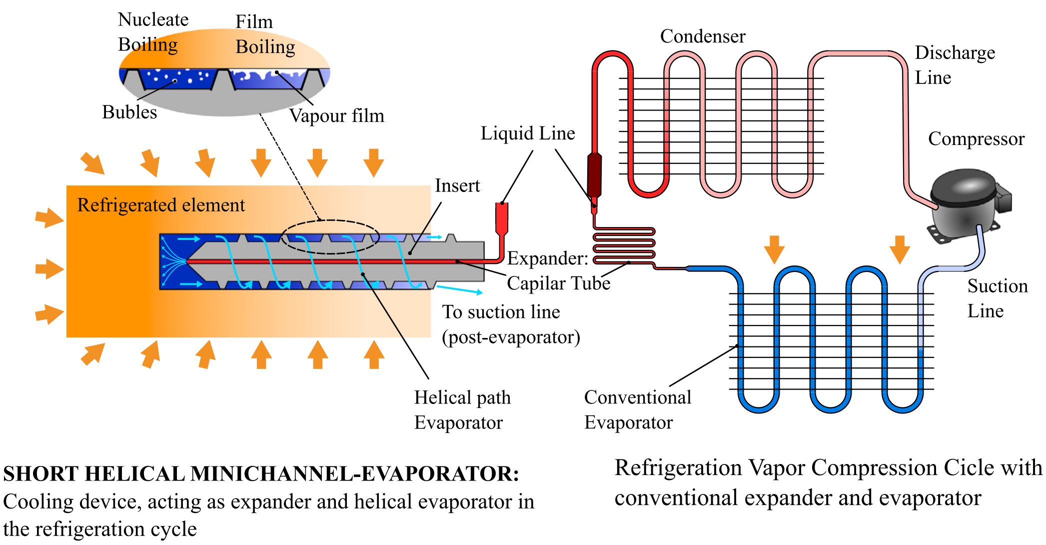

Fig. 1. Schematic sketch of a SHME in the refrigeration circuit.

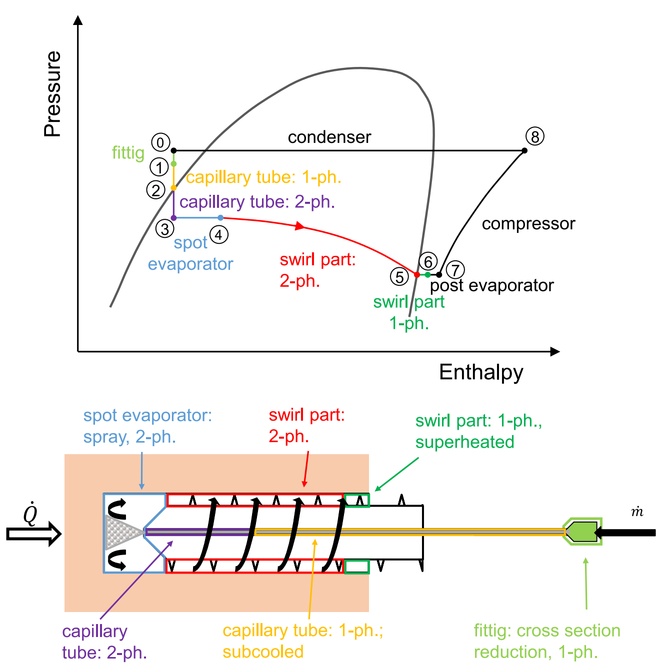

Fig. 2. Process steps in the SHME.

It is also promising for cooling high-performance processors due to its significant heat flux handling in limited spaces.

To fully utilize SHMEs, understanding the factors influencing CHF in flow boiling is crucial, especially considering the potential for sudden temperature surges beyond the CHF point. This knowledge is vital for future research aimed at optimizing SHME design and operation.

Over the past few decades, there has been a proliferation of empirical CHF correlations, particularly for water-cooled tubes. In fact, over 1000 methods are currently available [12]. This proliferation of methods reflects the inherent complexity of CHF mechanisms, as no single formula or theory can be universally applied to all CHF scenarios.

Predicting CHF under conditions with additional variables, such as non-uniform flow distributions, transients and asymmetric cross-sections, becomes significantly more complex. No existing correlation has been found that thoroughly addresses the unique geometry and phenomena specific to the SHME.

Hardik and Prabhu [13] study the CHF phenomena in helical coils, an area with limited previous research. Due to the curvature of these coils, the centrifugal force generates secondary fluid flows that may affect the heat transfer process and thus CHF in helical coils. This research compares new experimental CHF data with existing correlations found in the literature. It was found that correlations for helical coils work well for long coils, but not as effectively for short coils. In contrast, correlations for straight tubes are more universally applicable to all helical coils.

This work begins by discussing the concept and relevance of SHMEs and their construction and design principles. It then describes the experimental setup and test procedures for determining CHF in SHMEs, followed by a discussion on the mechanisms behind CHF and a presentation of a CHF model. The comparison of the CHF model results with the experimental data is conducted in the validation of the CHF model section. Once validated, the model is applied in conditions beyond the capacity of the experimental setup to enhance understanding of design parameters in these devices. The findings are comprehensively discussed, linking them to broader implications in the field. The study concludes with a summary of its main findings and contributions and suggestions for future research.

This paper aims to enhance the understanding of CHF in SHMEs, providing valuable insights for both academic and practical applications in thermal engineering.

2. Design of a SHME

For a more intuitive understanding, a simplified schematic of the design is shown in Fig. 1. The expansion as well as the evaporation of the refrigerant takes place in the SHME. The compression and condensation of the refrigerant is the same as in a standard refrigeration circuit.

The mean radius used for the SHME was measured to be $r = 1.92$ mm, as shown in Fig. 3, where P is the pitch, r is the mean radius of the screw and S is the engagement length.

At full engagement length, the maximum engagement is $S = 40$ mm. This results in a loss of 6.25 mm through the tip for each helical geometry or screw, so the effective engagement length is set at 33.75 mm for 100% engagement length.

The hydraulic diameter d_{hyd} is varied by using screws or helical evaporator geometries with different pitches. The helical geometries have been manufactured from an AlSi7Mg0.6 alloy using the micro casting process. Due to the constant installation space, the evaporator section is also reduced as the pitch increases, as shown in Fig. 4. Thus,

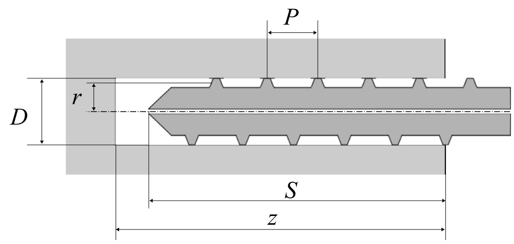

Fig. 3. Dimensions of the bore and helical geometry.

Table 2
The measured screw lengths, windings and the resulting pitches.

No.	Uncoiled Engagement length L in mm	Hydraulic diameter d_{hyd} in mm	Pitch P in mm
1.	180.720	0.835	2
2.	123.272	1.270	3
3.	79.086	1.488	5
4.	68.686	1.638	6
5.	61.572	1.807	7
6.	–	3.7	–

an SHME with a larger pitch has a shorter evaporator section than an SHME with a smaller pitch due to the installation space in the borehole (constant overall length S of the SHME). The variations in the pitch of the SHME are shown schematically in Fig. 4.

The relationship between the evaporator length L (uncoiled) and the total length S as a function of the pitch P and the mean radius r can be calculated as

$$L = \sqrt{P^2 + 4\pi^2 r^2} \cdot \frac{S}{P}. \tag{1}$$

Fig. 4 also shows the micro cast helical inserts with a pitch of $P =$ 2 mm on the left and $P = 7$ mm on the right. The pitch of these inserts is constant over the length of the component.

The bore for the screw or helical geometry has a depth of z = 45 mm and a diameter of $D = 4.5$ mm. Without a helical geometry (as in a spot evaporator [14]), the evaporation distance is $L = 40$ mm, and the hydraulic diameter is $d_{hyd} = 3.7$ mm, calculated by subtracting the outer diameter of the capillary tube from the bore diameter. This configuration, along with various helical geometries or screws, can be compared in Table 2. When helical geometries or screws are inserted, the evaporator distance increases due to the longer path of the refrigerant through the helix, while the hydraulic diameter decreases. Different pitches of these geometries or screws alter both the evaporator length and hydraulic diameter; smaller pitches lead to a smaller hydraulic diameter and longer evaporator length, while larger pitches increase the hydraulic diameter and shorten the evaporator length.

The hydraulic diameter is calculated [15] as

$$d_{hyd} = \frac{4 \cdot A}{U}. \tag{2}$$

Where A is the measured area in Fig. 5 and U is the perimeter of this area. The measured areas and perimeters are arithmetically averaged, the hydraulic diameter is calculated and the deviation is determined. Fig. 5 shows the hydraulic diameter for a helical insert with a pitch of 2 mm. The calculated values for different pitches can be seen in Table 2.

Previously, recessed geometries with a spot evaporator were used for cooling [14]. However, without this helical geometry, the evaporator length is significantly reduced. With a spot design, lower fraction of the refrigerant can be evaporated before reaching CHF. Consequently, further vaporization and superheating is needed in a secondary evaporator. By employing an SHME, higher fraction can evaporate before reaching CHF. This allows one more efficient cooling process and smaller secondary evaporator compared to a single point evaporator.

Table 3
Position of the thermocouples.

No.	Depth of borehole	Radial position
T_1	45 mm	5 mm
T_2	30 mm	5 mm
T_3	50 mm	5 mm
T_4	35 mm	5 mm
T_5	19 mm	central

3. Experimental setup and test procedure

This section details the experimental setup designed to measure the CHF in SHMEs. It covers the configuration of the setup, followed by a comprehensive description of the components and their functionalities. Subsequently, the data acquisition and control systems are explained. The refrigeration test bench for the SHME is basically a normal refrigerant cycle with a number of auxiliaries to control superheat, subcooling and condensing temperature. Difluoromethane, R-32 was chosen as refrigerant. This is an hydrofluorocarbon (HFC) with a low global warming potential of 675 and with an A2L flammability rating, which is favorable compared to hydrocarbons. In addition, R-32 is non-toxic and has thermodynamic properties that makes it suitable refrigerant fluid for SHME applications.

3.1. Experimental setup configuration

The experimental setup for investigating CHF in SHMEs is situated within a climate-controlled room maintained at a constant ambient temperature of 22 °C ± 0.5 °C. The setup consists of a closed loop refrigeration cycle and a dedicated measurement section, as illustrated in the flowchart of Fig. 8. A complete list of all components used in the setup is provided in Table 4.

3.2. Measurement section

The heart of the setup is the measurement section, which houses the capillary holder, the capillary tube itself, and the test carrier. The test carriers are fabricated from copper, with thermal conductivity $\lambda = 391 \frac{W}{m \cdot K}$.

A sectional view of the test carrier, which consists of a copper housing, is provided in Fig. 6. To accommodate the temperature measurements, the test carrier was carefully designed with five holes. These holes facilitate the integration of thermocouples, which serve as indispensable tools in the data acquisition strategy. For a better perspective, the exact locations of these thermocouples within the test body are shown in Fig. 7. Depths and positions of the boreholes are detailed in Table 3. Temperature sensors are positioned to monitor fluid temperature and pinpoint the CHF.

3.3. Refrigeration cycle

As shown in Fig. 8 the SHME is part of a closed loop refrigeration cycle including a compressor (11), condenser (12) receiver (13), subcooler (14) and mass flow meter (10). Thermodynamic variables are monitored by pressure gauges (8), and temperature sensors (9). The thermal power to the SHME is supplied by an electric heating jacket (4) mounted on the cylindrical surface of the test carrier (2).

Sensors are strategically placed throughout the test stand and measurement section to record various parameters. Additionally, the cooling load applied to the measurement section via the heating jacket can be precisely controlled and adjusted.

After passing through the evaporator test section (1) (Fig. 8) temperature and pressure of the refrigerant are measured to determine its thermodynamic state exiting the measurement section. Before entering the oil-free two-piston compressor (11), the refrigerant is routed

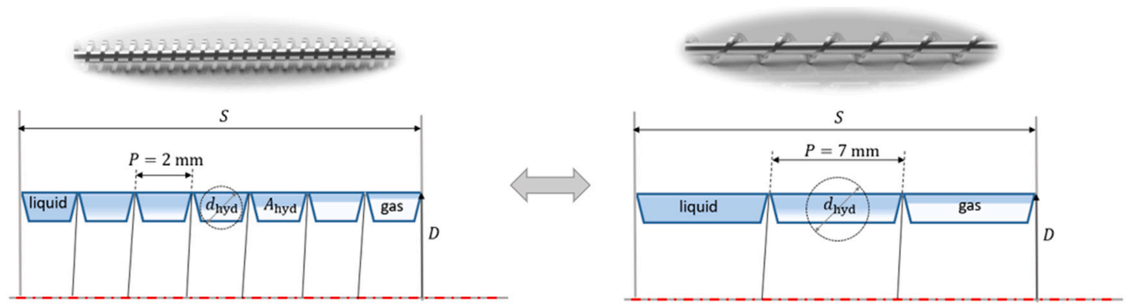

Fig. 4. Illustration of the experimental variations.

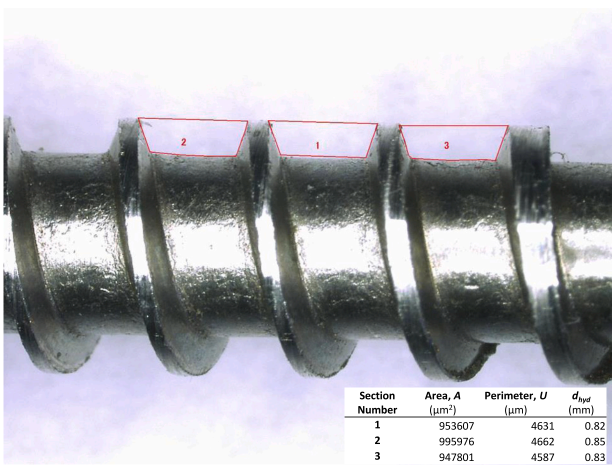

Fig. 5. Flow cross-sectional areas and wetted perimeters for a screw with 2 mm pitch.

Table 4
Components of the test setup.

Designation	Manufacturer	Value range
SHME and capillary support	In-house production	
Pressure sensors	Endress+Hauser	0–1 MPa
Coriolis mass flow meter	Endress+Hauser	0–30 kg/h
Thermostat, subcooler	Peter Huber GmbH	−25–150 °C
Post evaporator	In-house production	
Compressor	REFCO	33 kg/h; gas-phase
Refrigerant receiver	ESK Schulze	
Thermostat, condenser	Peter Huber GmbH	−40–250 °C
Power meter	HAMEG	1 mW–8 kW
DC power supply	Gwinstek	0–30 V, 3 A
Data acquisition	National Instruments	32 bit
Computer	Dell	
Thermocouples Type J	TMH GmbH	−50–150 °C

through a plate heat exchanger (15). This heat exchanger is coupled to a water-glycol circuit that serves to evaporate and superheat the refrigerant, ensuring only gaseous refrigerant enters the compressor. This plate heat exchanger acts as an additional evaporator and functions as a safety feature. It allows the SHME to operate in flooded conditions while maintaining a constant superheat of 15 K across all operating states. Consistent superheat during a test series is crucial for maintaining consistent test conditions.

After the compressor, condensation takes place in a plate heat exchanger (12) connected to a second thermostat via a water-glycol circuit. In addition to temperature and pressure measurements within the refrigeration cycle at various points, the inlet and outlet temperatures of the water-glycol coolant for the auxiliary units (post-evaporator and condenser) are also monitored. The outlet temperature of the thermostat is adjusted based on the outlet temperature of the refrigerant from the plate heat exchanger to achieve the desired condensing pressure within the circuit.

After condensation, the refrigerant is directed to a receiver (13). The liquid refrigerant then flows through a finned tube heat exchanger (14). Here, a water-glycol mixture again serves as the heat transfer medium for another thermostat that controls the subcooling temperature. The subcooling process is controlled and measured by the temperature difference between the refrigerant temperature exiting the receiver and the liquid temperature entering the capillary. All temperature measurements are conducted using type J thermocouples.

Within the system, after traversing the heat exchanger for subcooling adjustment, the mass flow rate and density of the liquid refrigerant are measured using a Coriolis mass flow meter (10). Temperature and pressure are measured with a thermocouple and pressure sensor before the refrigerant enters the capillary, allowing for the calculation of its thermodynamic state.

The liquid lines have an internal diameter of 4 mm to minimize pressure losses, which are measured at approximately 200 mbar with a system pressure of $p_c = 9.7$ bar. The suction line has a diameter of 9 mm, and all pipes are constructed from stainless steel 1.4301. These pipes are insulated with 10 mm thick Armaflex foam.

3.4. Data acquisition and processing

Data acquisition and processing for the test stand are facilitated by A/D converters from National Instruments (NI) and LabVIEW software. The data acquisition and processing schematic can be found in Fig. 9, and the corresponding components are listed in Table 4. All thermocouples employed in the test stand are connected via A/D converters (NI-9211 and NI-9213). These converters offer integrated cold junction compensation and operate on a 24-bit basis, enabling a maximum resolution of 0.02 K. This translates to a calibrated accuracy of 0.1 K across the entire temperature measurement chain. The pressure sensors and the mass flow meter transmit signals captured by the A/D converter NI-9203. These sensors provide the signals as analog current signals within the range of up to 20 mA. The A/D converter's 16-bit sampling rate provides sufficient resolution to accommodate the tolerances of the various sensors used in the setup.

3.5. Control of the test stand

A custom-programmed LabVIEW software application serves as the central control hub for the test stand. This software interacts with various valves and a control card (NI-9263) to regulate critical parameters within the system. The control card generates a ±10 V voltage signal with 16-bit resolution, enabling precise control over the connected components. The software manages the power delivered to the electrical heating jacket surrounding the test carrier. Feedback from the heating power consumption enables closed-loop control, ensuring accurate power delivery. Both the subcooling and condensation pressure thermostats are directly integrated into LabVIEW. The software allows for either automated control based on pre-defined setpoints or

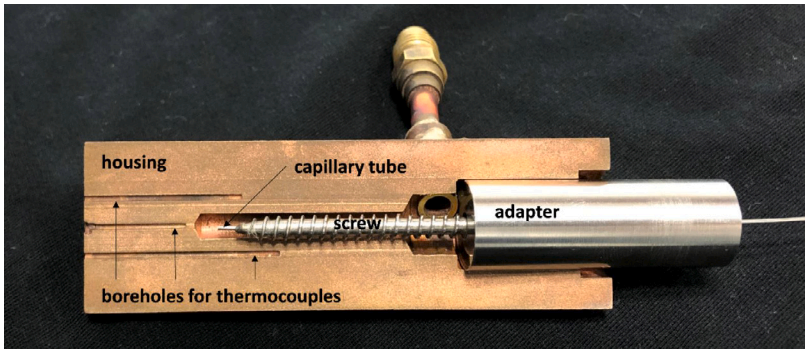

Fig. 6. SHME test carrier design and function.

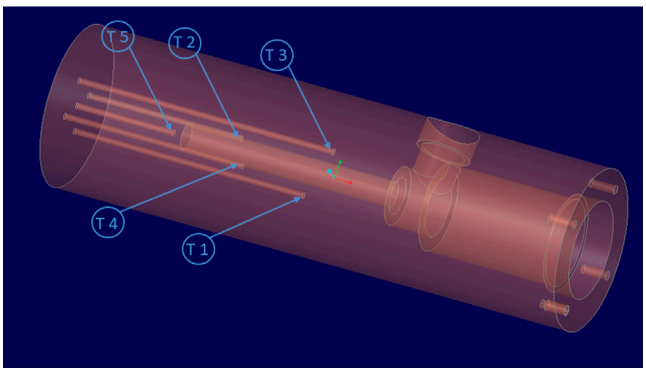

Fig. 7. Positions of the thermocouples in the test carrier.

manual temperature adjustments via the control panel. The sampling rates and control loop speeds within the program are user-configurable. This flexibility allows for fine-tuning the control system based on the specific requirements of each experiment. Through preliminary testing, a sampling rate of 2 Hz was determined to be sufficient for capturing all relevant processes within the test stand.

3.6. Test procedure

The initial step involves operating the test bench at a power input of 120 W for a duration of one hour. This ensures the establishment of steady-state conditions within the system, which is crucial for obtaining reliable data on pressure and temperature dynamics throughout the experiment. The following key parameters are meticulously controlled and maintained throughout the testing process:

- Condensation pressure (p_c): Maintained at a constant value of 9.7 bar, corresponding to a condensation temperature of 5.63 °C.
- Evaporation pressure (p_o): Varied strategically between 3.08 bar and 3.55 bar. This variation is dependent on factors such as the length of the evaporator section and the hydraulic diameter.

To minimize heat dissipation to the surrounding environment and ensure that the thermal energy is directed towards the test carrier, both the carrier itself and the encompassing electrical heating jacket are well isolated and enclosed within a plastic box. The CHF measurement is conducted under steady-state conditions within the cooling circuit. The power input is progressively incremented by 10 Watts every 900 s. This incremental increase continues until the CHF point is reached. The CHF's onset is identified by a rapid surge in all the measured temperatures, signifying an important shift in the system's thermal dynamics. In the experimental determination of the CHF in SHMEs, the key measured variables included the evaporation pressure p_o, condensation pressure p_c, mass flow rate $\dot{m}$, electrical power $\dot{Q}_{el}$ of the heating band and temperatures recorded by thermocouples T_1 to T_5. At the end of the test series, the analyzed data were systematically plotted on graphs to ensure a clear presentation of the results. For the sake of clarity, the electrical power $\dot{Q}_{el}$ has been plotted against the temperatures recorded by thermocouples T_1 to T_5.

The graph in Fig. 10 clearly illustrates the abrupt transitions in the recorded temperatures caused by exceeding the CHF, starting from a power input of 260 W. The study includes a total of 32 such experiments, using swirl inserts with different hydraulic diameters ranging from 0.84 mm to 3.7 mm. The experimental raw data is available in one Mendeley dataset.

The method proved to be very effective in determining the CHF. When the CHF is exceeded, there is a noticeable and sudden increase in temperature from one power increase to the next, as clearly shown in Fig. 10. In contrast, when operating in the nucleate boiling regime, an increase in power results in only a small oscillation in the observed temperature. The observed abrupt transition in temperatures, together with changes in their relative sequence, are indicative of changes in the heat flux pattern across the test body.

Fig. 10 presents an interesting observation: while CHF is reached, the wall temperature rise is a slow process, taking approximately 1500 s. This behavior deviates significantly from typical scenarios involving water as the working fluid and different configuration of the solid refrigerated element, where CHF triggers a rapid rise in wall temperature, often within 60 s. Our test carrier is fabricated from copper, a material with significantly higher thermal conductivity compared to the materials commonly used in evaporator components of power plants (such as stainless steel). The ratio of the solid mass refrigerated compared to the heat transfer surface is also very different making the transient periods in our system significantly longer.

Besides, the experimental setup employs high mass flux density and high turbulence. These conditions can influence the observed trend, since the initial formation of a local vapor film can be disrupted or penetrated by surges of still-liquid refrigerant or refrigerant droplets. The helical geometry of the SHME introduces backflow and secondary flow effects within the working fluid. These complex flow patterns can disrupt the heat transfer process, further delaying the temperature increase after CHF is reached.

As a result, it takes about 1500 s for the temperature to reach a very high level in the positions of the thermocouples in the test carrier, compared to the 60 s typically observed in different experiments like those conducted by Nukiyama or in power plants.

4. CHF in helical evaporators

Despite the mentioned correlations, it is important to remember that they do not perfectly account for the phenomena that occur within a SHME, which remains a challenge for accurate prediction of CHF. Given the intricacies involved in predicting the CHF using correlations, Groeneveld and his associates introduced an innovative approach in the

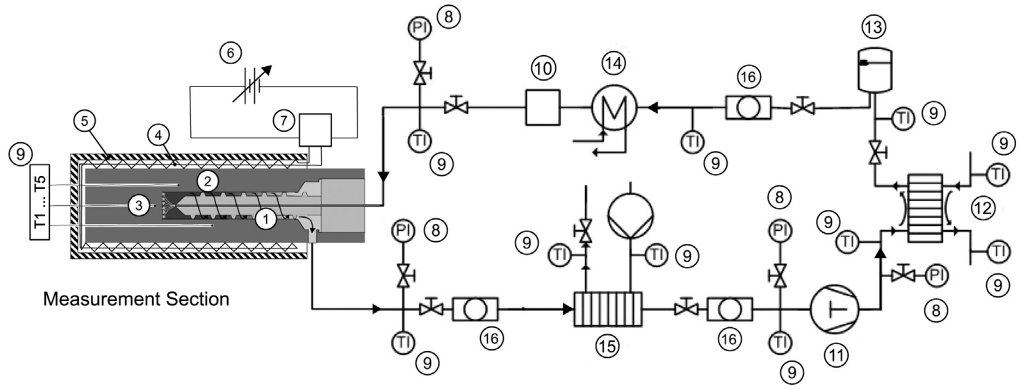

1	SHME	5	Heating jacket insulation	9	Temperature sensors	13	Refrigerant receiver
2	Test carrier	6	DC Power source	10	Coriolis mass flow meter	14	Subcooler
3	Test carrier thermocouples	7	Power meter	11	Compressor	15	Post-evaporator
4	Electrical heating jacket	8	Pressure sensors	12	Condenser	16	Sight glass

Fig. 8. Refrigeration Cycle Diagram of the experimental setup.

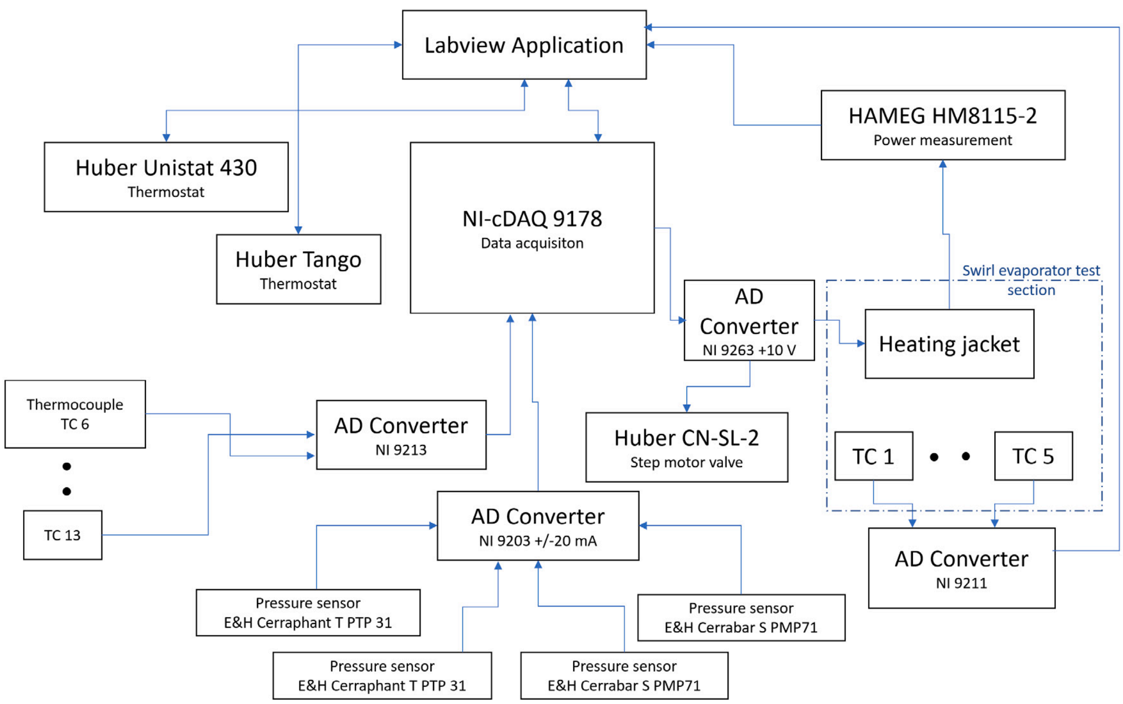

Fig. 9. Data Acquisition and Processing Schematic.

form of a look-up table, essentially a normalized database, to predict the CHF [12]. This table facilitates the prediction of CHF as a function of the refrigerant mass flux (G), pressure (p), and vapor quality (x), as represented by the equation:

$$\mathrm{CHF} = f(G,\, p,\, x). \tag{3}$$

Groeneveld et al. conducted extensive research on the CHF for flow boiling of water in vertical tubes of 8 mm diameter. Their study examined over 30 000 data points with varying parameters. The intermediate values are generated through interpolation. To extend the application to tubes of different diameters, they proposed the following extrapolation equation:

$$\mathrm{CHF} = \frac{\mathrm{CHF}_{8\,\mathrm{mm}}}{\sqrt{\frac{d_{\mathrm{hyd}}}{8\,\mathrm{mm}}}}. \tag{4}$$

Groeneveld's method offers several advantages over correlation-based CHF prediction methods, such as:

- User-friendly operation
- Broad application range
- No need for iteration
- Foundational basis on an expansive database
- Eliminates the necessity to select from various available CHF prediction methods

Owing to the vast number of data points, Groeneveld's look-up table could be considered the universal approach among CHF determination methods [16–21], providing accurate CHF estimation in SHMEs. The Groenveld look-up tables, originally developed for water, offer the potential for application to other refrigerants through fluid-to-fluid scaling. While this approach is theoretically sound, practical validation is essential for any new refrigerant being considered. As suggested by

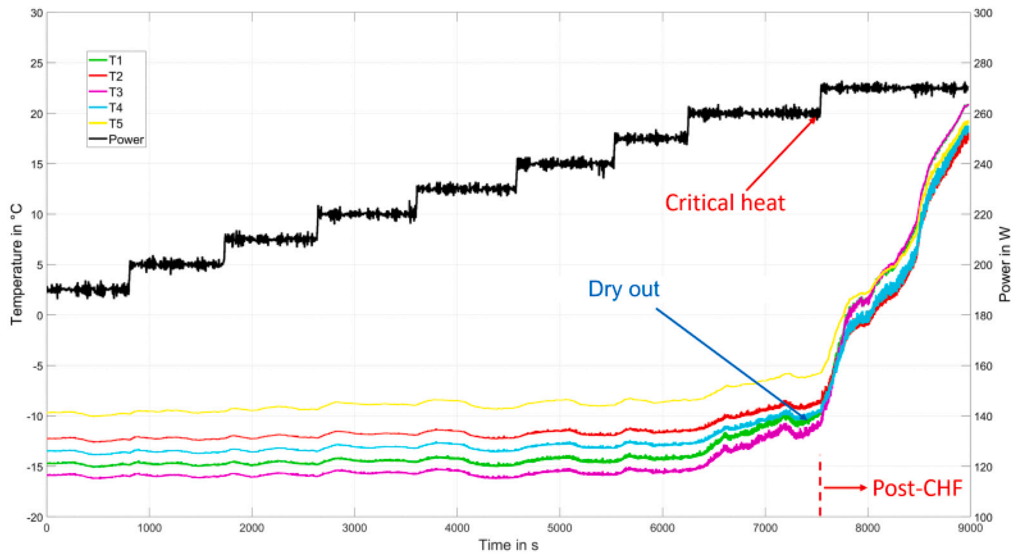

Fig. 10. Determining the CHF through the course of the temperature curves.

Pioro et al. [21], experimental validation is crucial to ensure the reliability and accuracy of these tables when applied beyond their initial scope with water. This validation process will help to fine-tune the scaling method to suit the unique properties of different refrigerants, thereby extending the usefulness of the Groenveld tables in different thermal systems.

4.1. Modeling CHF in SHMEs

As refrigerant flows through an evaporator, the refrigerant evaporates, resulting in a gradual increase in vapor quality x. This vapor quality increases until it can reach a critical point, beyond which a local vapor film forms. This phenomenon marks the onset of CHF. At this point, the vapor film acts as an insulating layer, drastically reducing heat transfer compared to the earlier nucleate boiling phase. The critical point in steam quality, where the CHF is reached, is called x_{crit}.

As the externally introduced heat is concentrated on a decreasing wetted surface area, the heat flux increases, accelerating the transition to CHF at a lower critical steam quality. Subsequently, this growing vapor film extends upstream and eventually covers significant portions of the evaporator with this insulating layer. Thus, the critical vapor quality at which CHF is first locally exceeded serves as a key parameter in determining the onset of CHF throughout the system.

In the context of SHMEs, the region towards the end of the evaporator section, is critical. It is characterized by low vapor content and is identified as the limiting factor for heat transfer and is often the location where CHF occurs. To calculate CHF in these systems, a modified method proposed by Groeneveld [12] is used. This approach recognizes that once CHF is locally reached at a given vapor content, it effectively extends to the entire system.

The formation of an insulating vapor film at the local CHF point redistributes the electrical heat introduced into the system to the remaining liquid-wetted surface. Although the power remains constant, the heat flux increases due to the reduced heat absorbing surface area. The remaining wet surface can only absorb heat through nucleate boiling, while the area under the vapor film becomes effectively insulated.

However, this method has its limitations, primarily because the steam content determination is inextricably linked to the CHF determination. The CHF correlation, originally developed for straight pipes, has been adapted for use in spiral flows, as suggested by Hardick and Pradu [13]. Their research suggests that correlations for straight pipes may be applicable to spiral flows, thus providing an avenue for refined CHF prediction in complex geometries such as SHMEs. In the evaporator section a certain heat flux $\dot{Q}_{swirl}$ is absorbed. This quantity is determined by the specific enthalpy of evaporation Δh_{vap}, the mass flow rate $\dot{m}$, and the change in vapor quality between the inlet (x_{in}) and outlet (x_{out}), defined by the following equation:

$$\dot{Q}_{swirl} = \dot{m} \cdot \Delta h_{vap} \cdot (x_{out} - x_{in}). \tag{5}$$

The inlet vapor quality can be calculated using the specific enthalpies h as demonstrated in the subsequent equation:

$$x_{in} = \frac{h_{in} - h_l}{\Delta h_{vap}}. \tag{6}$$

By leveraging Groeneveld's look-up table, the local CHF can be found at the current vapor quality x. If the exit vapor quality x_{out} for x is used, the remaining "reserve" can be ascertained before CHF is reached. This is possible since the CHF reduces with the increase in quality [12] and is, therefore, first achieved at the evaporator outlet.

The exit vapor quality x_{out}, which corresponds to the vapor quality at which the CHF occurs, is referred to as the critical vapor quality $x_{crit.}$. This can be expressed as follows:

$$\mathrm{CHF}_{swirl} = f(p, G, x_{crit}, d_{hyd}) \tag{7}$$

where

$$G = \frac{4 \cdot \dot{m}}{\pi \cdot d_{hyd}^2}. \tag{8}$$

The maximum transmittable heat flux, $\dot{Q}_{max}$, is calculable by multiplying CHF_{swirl} by the heat transferring area A_{swirl}, which is the lateral surface area of the borehole defined by its length and diameter $A_{swirl} = \pi \cdot D \cdot z$.

$$\dot{Q}_{max} = \mathrm{CHF}_{swirl} \cdot A_{swirl}. \tag{9}$$

The critical vapor quality $x_{crit.}$ acts as an indicator that reveals whether the CHF is reached and at which power the departure from nucleate boiling (DNB) happens, or whether it occurs at all. Provided the outlet vapor quality x_{out} is lower than the critical vapor quality x_{crit}, the entire swirl region remains within the nucleate boiling range, resulting in a correspondingly low wall superheat ($T_w - T_{sat}$) as shown in Fig. 11(a).

When the exit vapor quality corresponds to the critical vapor quality, a thin insulating vapor film forms at the evaporator exit. This

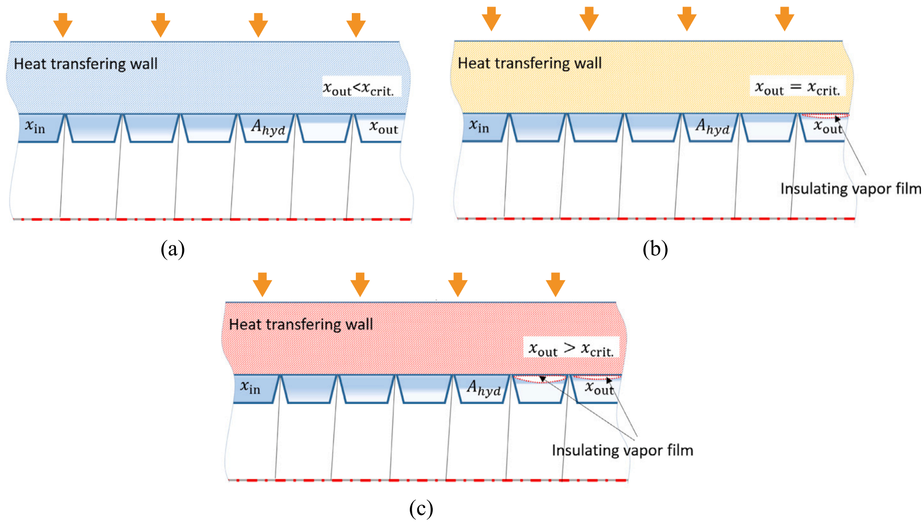

Fig. 11. Formation of the vapor film: (a) $x_{out} < x_{crit}$; (b) $x_{out} = x_{crit}$; (c) $x_{out} > x_{crit}$.

occurrence results in a slight increase in wall superheat, as depicted in Fig. 11(b).

The formation of this insulating film hinders heat transfer at this specific point, while the average heat flux remains unchanged. Consequently, the heat flux at the remaining upstream heat transfer surface elevates, leading to a continuous increase in wall superheat and eventually resulting in film boiling in the further upstream areas of the swirl path. In essence, the insulating vapor film spreads from the outlet upstream along the evaporator section, as depicted in Fig. 11(c).

The insulating vapor film that emerges at $x_{out} = x_{crit.}$ can be conceptualized as the "nucleus" of film boiling and the precursory sign of the cooling process collapse. The onset of the CHF and the expansion of the vapor film follow this point.

The refrigerant's exit vapor quality, x_{out}, at the conclusion of the evaporator section is the critical parameter x_{crit}, used to assess whether or not CHF occurs. The CHF occurs when $x_{out} = x_{crit}$. By inserting

$$x_{out} = x_{crit} \tag{10}$$

into Eq. (5), we can calculate $\dot{Q}_{crit}$ as:

$$\dot{Q}_{crit} = \dot{m} \cdot \Delta h_{vap} \cdot (x_{crit} - x_{in}). \tag{11}$$

By setting Eq. (9) equal to Eq. (11), the maximum heat flux that can be transferred under the prevailing conditions is determined,

$$\mathrm{CHF}_{swirl}(p, G, x_{crit.}, d_{hyd}) \cdot A_{swirl} = \dot{Q}_{crit} \tag{12}$$

is obtained and the heat flux can be computed with

$$\mathrm{CHF}_{swirl} = \frac{\dot{Q}_{crit}}{A_{swirl}} \tag{13}$$

or with Eq. (7), given that x_{crit} is known. Fig. 12 illustrates the curve of $\dot{Q}_{swirl}$ and $\dot{Q}_{crit}$ as a function of the outlet vapor quality x_{out}. The critical vapor quality x_{crit} can be discerned from the intersection of these two curves, where the CHF is achieved.

In Fig. 12 the heat flux $\dot{Q}_{swirl}$ is represented by the black curve. It is calculated using Eq. (5). The blue curve represents the maximum possible heat flux $\dot{Q}_{crit}$, calculated using Eq. (9) and Eq. (11).

The critical vapor quality x_{crit} can be determined graphically by the intersection of the black and blue curves, indicating the onset of CHF. For values of x_{out} less than x_{crit}, $\dot{Q}_{crit}$ is greater than $\dot{Q}_{swirl}$, so CHF is not reached and the entire swirl region is in the nucleate boiling region. Conversely, when x_{out} exceeds x_{crit}, $\dot{Q}_{swirl}$ becomes larger than $\dot{Q}_{crit}$, which means that the CHF is reached, leading to a transition to film boiling.

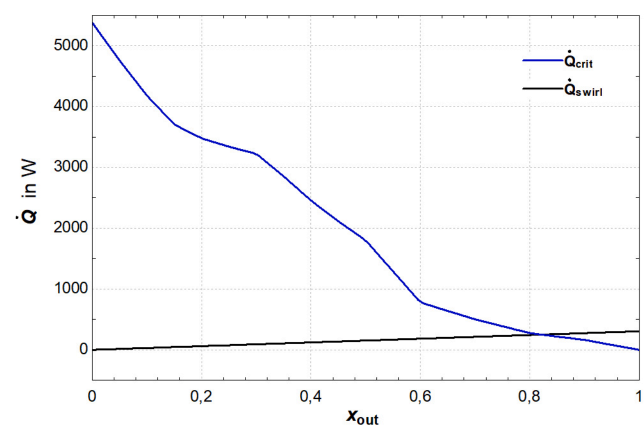

Fig. 12. Curve of the heat flux $\dot{Q}_{swirl}$ and the maximum possible heat flux $\dot{Q}_{crit}$ as a function of the outlet vapor quality x_{out}.

In practical applications, an iterative procedure is often used to calculate x_{crit}. This involves adjusting the value of x_{crit} and recalculating the heat flux $\dot{Q}_{swirl}$ and $\dot{Q}_{crit}$ until the difference between the two is less than a predetermined tolerance.

Once x_{crit} is known, the maximum power before the onset of CHF can be determined:

$$\dot{Q}_{crit} = \dot{Q}_{max}. \tag{14}$$

This provides a limit to the operating conditions of SHMEs. Operating SHMEs at power levels higher than $\dot{Q}_{max}$ would result in a transition from nucleate boiling to film boiling, thereby significantly reducing the heat transfer efficiency.

Therefore, understanding and correctly calculating the CHF and the corresponding critical vapor quality in the swirl region plays an important role in the design and operation of efficient and safe refrigeration systems.

It is important to remember that the accuracy of these calculations is highly dependent on the quality of the correlations or look-up tables used for CHF, as well as the accuracy of the refrigerant property data. These parameters should be carefully validated against experimental data to ensure the reliability of the predicted CHF and critical vapor quality.

Table 5
Absolute and relative factors of the measuring equipment.

Designation	Measured quantity	Calibrated range	Value range	Units	Factor
Cerabar S PMP71	p_c, p_o	0–25	0–10	MPa	±0.05% of the measuring range
Promass 83A	$\dot{m}$	0–25	0–30	$\frac{kg}{h}$	±0.1% of the measured value
Ministat 125-cc	T_{sub}	−25–450	−25 - 450	°C	±0.1 K
Unistat 430	T_c	−50–90	−4–250	°C	±0.01 K
HM 8115-2	P	0–500	0.01–8	W	±0.8% of the measured value
Thermocouple Type J	T_o, T_c, T_1–T_5	−50–200	−50–150	°C	±0.1 K

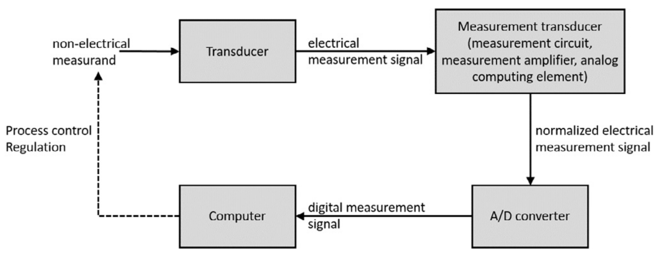

Fig. 13. Elements of a measuring system [23].

5. Error analysis

Pursuant to DIN 1319 [22], the fundamental objective of measurements is the identification of the actual value. Since achieving a true value is practically impossible due to inherent measurement inaccuracies, there will invariably be deviations present in all measurements. These deviations are articulated as error bars or bands surrounding the true value, attributable to various factors such as:

1. Conversion errors in the measuring chain
2. Calibration inaccuracies of the measurement apparatus
3. Manufacturing variances
4. Unaccounted external influences
5. Human error in measurement, among others.

Refer to Fig. 13 for a representation of a measurement chain comprising numerous elements, each potentially introducing uncertainties that could lead to deviations from the actual measured value.

Uncertainties in transducers can be categorized into relative and absolute factors. The relative factor e_{rel}, being dimensionless, is defined in relation to the maximum measuring range of a device, as given by

$$e_{\mathrm{rel}} = \frac{x_{\mathrm{m}} - x_{\mathrm{real}}}{x_{\mathrm{m}}}. \tag{15}$$

In this context, it is crucial to note that the variable x denotes a measured value, not vapor quality. The absolute uncertainty, e_{abs}, represents the disparity between the measured (x_{m}) and actual values (x_{real}), described mathematically as

$$e_{\mathrm{abs}} = x_{\mathrm{m}} - x_{\mathrm{real}}. \tag{16}$$

The specific uncertainty factors employed within the experimental setup are listed in Table 5.

For computational purposes involving sums and differences, absolute uncertainties can be summed up, while relative uncertainties are multiplied in cases of product or quotient calculations. Total measurement uncertainty (e) is obtained by the aggregate of static (e_{stat}) and dynamic uncertainties (e_{dyn}), expressed as

$$e = e_{\mathrm{stat}} + e_{\mathrm{dyn}}. \tag{17}$$

Dynamic uncertainties emerge when there is a temporal displacement between the input and output of a measured value in the measurement chain. However, these can be overlooked in this experiment due to the stationary conditions maintained throughout the measurement process.

Static uncertainties manifest from stochastic variations (e_{sto}) and systematic measurement deviations (e_{sys}), combining to give the measurement uncertainty,

$$e_{\mathrm{stat}} = e_{\mathrm{sto}} + e_{\mathrm{sys}}. \tag{18}$$

Systematic uncertainties, usually constant offsets, can be mitigated through precise calibration of measurement techniques. Stochastic uncertainties are inherently more challenging to ascertain due to influences such as:

- Errors in the measurement chain
- Sensor noise
- Environmental variables
- Interpretation discrepancies, among others.

By conducting repeated measurements and calculating the average, stochastic factors can be mitigated. Relative elements of the measurement means are embedded within these stochastic components. Utilizing normal distributions, such as the Gaussian normal distribution, aids in the countering of these stochastic factors.

The measurements from all sensors were sampled at a frequency of 2 Hz, and an average value was generated from 1200 individual readings. This average symbolizes the refined measurement outcomes of this study, corresponding to a ten-minute measurement duration under consistent conditions.

The mathematical representation of averaging the individual measurements $\bar{x}_i$ is formulated as:

$$\bar{x}_i = \frac{1}{n}\sum_{j=1}^{n} x_{ij}. \tag{19}$$

Moreover, the empirical standard deviation, symbolizing the mean square deviation from the arithmetic mean, is described by:

$$s = \sqrt{\frac{1}{n-1}\sum_{j=1}^{n}\left(x_{ij} - \bar{x}\right)^2} \tag{20}$$

From subsequent computations, the uncertainty u can be discerned by confining finite measured values, given by:

$$u = \frac{1}{\sqrt{n}} \cdot s \tag{21}$$

Extreme values, x_{min} and x_{max}, are also computed from the 1200 values of a measurement under unvaried conditions.

The dependent variable, denoted as $\bar{y}$, a function of $\bar{x}_i$, is expressed as:

$$\bar{y} = f(\bar{x}_i). \tag{22}$$

Table 6
Test runs for CHF.

Test run No.	d_{hyd} in mm	$\dot{m}$ in kg h^{-1}	p_{o} in bar	$\dot{Q}_{\text{crit;mea}}$ in W	CHF_{sim} in kW m^{-2}	CHF_{mea} in kW m^{-2}
1	0.84±0.1	3.12±0.0031	3.37±0.026	260±5	335.16±45.97	368.01±7.092
2	0.84±0.1	2.99±0.0029	3.25±0.026	254±5	327.16±44.66	360.76±7.092
3	0.84±0.1	3.12±0.0031	3.37±0.026	260±5	335.17±45.97	368.01±7.092
4	0.84±0.1	2.98±0.0029	3.18±0.025	265±5	327.10±45.97	375.09±7.092
5	1.00±0.1	3.20±0.0032	2.00±0.016	265±5	372.10±46.06	375.09±7.09
6	1.00±0.1	3.25±0.0032	2.00±0.016	272±5	375.43±46.65	384.99±7.09
7	1.00±0.1	2.85±0.0028	1.90±0.015	270±5	348.13±45.62	382.17±7.09
8	1.00±0.1	2.67±0.0026	1.80±0.014	263±5	341.74±46.80	372.26±7.09
9	1.00±0.1	2.97±0.0029	1.80±0.014	265±5	357.74±45.81	375.09±7.09
10	1.27±0.1	3.05±0.0030	3.26±0.026	249±5	387.18±48.69	352.44±7.09
11	1.27±0.1	3.22±0.0032	3.17±0.025	259±5	405.71±51.13	367.65±7.09
12	1.27±0.1	3.13±0.0031	3.35±0.026	240±5	395.09±49.73	339.70±7.09
13	1.27±0.1	3.05±0.0030	3.28±0.026	237±5	387.20±48.69	336.69±7.09
14	1.27±0.1	3.22±0.0032	3.17±0.025	259±5	405.71±51.13	367.65±7.09
15	1.49±0.1	3.01±0.0030	3.22±0.025	241±5	387.06±48.57	341.47±7.09
16	1.59±0.1	3.00±0.0030	2.00±0.016	263±5	402.39±50.46	372.25±7.09
17	1.59±0.1	2.99±0.0030	2.00±0.016	253±5	402.39±50.46	358.11±7.09
18	1.64±0.1	3.04±0.0030	3.21±0.025	260±5	394.36±49.45	368.01±7.09
19	1.64±0.1	2.96±0.0029	3.17±0.025	260±5	385.35±48.32	368.01±7.09
20	1.64±0.1	3.12±0.0031	3.33±0.026	260±5	401.87±50.40	368.01±7.09
21	1.69±0.1	3.00±0.0030	1.95±0.015	265±5	403.99±50.65	375.08±7.09
22	1.69±0.1	3.02±0.0030	1.95±0.015	257±5	403.99±50.65	363.76±7.09
23	1.69±0.1	2.98±0.0030	1.95±0.015	250±5	403.99±50.65	353.85±7.09
24	1.78±0.1	3.02±0.0030	1.95±0.015	280±5	404.57±50.78	396.32±7.09
25	1.78±0.1	3.00±0.0030	1.95±0.015	263±5	404.57±50.78	372.25±7.09
26	1.81±0.1	2.99±0.0029	3.20±0.025	250±5	391.04±49.03	353.85±7.09
27	1.81±0.1	3.03±0.0030	3.23±0.025	250±5	395.35±49.57	354.03±7.09
28	1.81±0.1	2.98±0.0029	3.19±0.025	250±5	389.98±48.89	353.85±7.09
29	1.81±0.1	3.11±0.0031	3.33±0.026	260±5	403.24±50.56	368.01±7.09
30	3.70±0.1	3.20±0.0032	1.90±0.015	263±5	393.11±37.03	372.25±7.09
31	3.70±0.1	2.92±0.0029	1.90±0.015	250±5	359.76±32.96	353.85±7.09
32	3.70±0.1	2.88±0.0028	1.87±0.014	245±5	354.91±32.18	346.78±7.09

This calculation aims to ascertain the propagation of uncertainties in each measured variable x to the computed quantity y, where the partial differential $\partial\bar{y}$ epitomizes the uncertainty in the variables, expressed as:

$$\partial\bar{y} = \sqrt{\sum_{i=1}^{n}\left(\frac{\partial y}{\partial x_i}|_{\partial\bar{x}_i}\partial\bar{x}_i\right)^2}. \tag{23}$$

To evaluate uncertainties associated with CHF, a function incorporated in the Engineering Equation Solver (EES) was utilized. The uncertainties were calculated to be less than 15% for the largest deviation. The uncertainties specific to each test run for the validation of the model are delineated in Table 6.

6. Validation of the CHF model

In order to improve the understanding of the CHF in a SHME, a rigorous comparative evaluation of simulated and empirical test results has been undertaken, with particular emphasis on the verification of the CHF model. The CHF model plays a crucial role in predicting the thermal behavior of the system and therefore its validation is of paramount importance.

This study included several experimental tests where simulation results were carefully compared with corresponding empirical data. A comprehensive list of these tests is given in Table 6. The test runs cover a range of operating conditions, providing a robust data set for comparative analysis.

The analysis revealed a reasonably strong agreement between simulated and measured values, as shown in Fig. 14. This congruence not only validates the CHF model, but also confirms its suitability for predicting system behavior under different scenarios.

The results were further quantified using statistical measures such as Mean Absolute Error (MAE), Mean Error (ME) and Deviation (Dev), which was $8.51\,\text{kW m}^{-2}$, $-4.71\,\text{kW m}^{-2}$, and $8.77\,\text{kW m}^{-2}$ respectively. These metrics reflect the accuracy of the simulation model, with the MAE and Dev providing insight into the average size of the errors, while the ME indicates whether the model tends to over- or underestimate the actual values. In this case, a negative ME indicates a slight tendency for the model to underestimate the real world measurements.

In particular, 96.8% of the simulated values fell within an error band of 15%, demonstrating a high degree of accuracy in the simulation results. This is a significant finding that emphasizes the reliability and precision of the CHF model for predicting thermal performance in the SHME system. It confirms the usefulness of the model for future predictive studies, simulations and for potentially informing system design and operation strategies.

The consistency between simulation results and empirical observations lends credibility to the model and highlights its robustness. It is worth noting, however, that while the model has demonstrated significant accuracy, the presence of some errors underscores the importance of continued refinement. Future work could focus on reducing the observed deviation, improving the accuracy of the model and exploring its limits under more diverse or extreme conditions.

7. Extension and application of the CHF model

The CHF model developed and elaborated in this study is based on an empirically constructed data look-up table. This data-driven approach allows the model to be applied to scenarios beyond the parameters explicitly investigated in the experimental study. The model's ability to extrapolate from known data points makes it a valuable tool for gaining insights into CHF behavior under conditions that were not directly measurable due to the limitations of the experimental setup.

While the experimental setup could not capture the full range of parameters relevant to CHF, the model's ability to simulate these conditions provides valuable insights into system behavior. This simulation capability enables researchers to explore the impact of factors that were not directly measurable during the experiments, such as extreme operating conditions or complex geometries.

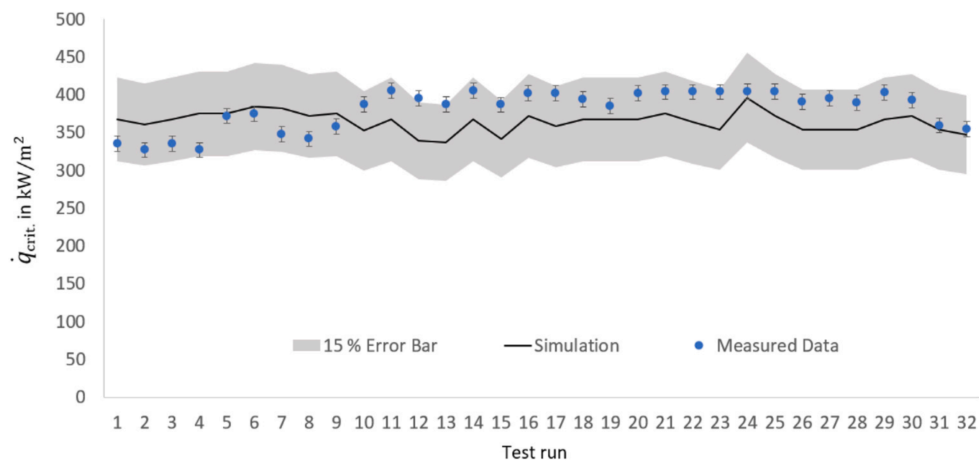

Fig. 14. Comparison of the measured and simulated CHF.

In this sense, the CHF model serves as a complementary tool to experimental investigations, expanding the scope of knowledge beyond the confines of the physical setup. By leveraging the model's extrapolation capabilities, researchers can gain a more comprehensive understanding of CHF under a wider range of conditions.

It is noteworthy, and confirmed by all three figures 15–17, that the CHF escalates with the mass flow rate (and hence the mass flux), a phenomenon widely recognized in the existing literature [2,24–27].

7.1. Impact of mass flow rate and geometric parameters on CHF

Fig. 15 illustrates the influence of the hydraulic diameter (d_{hyd}) on the CHF at different mass flow rates. A clear hydraulic diameter optimum can be seen at higher mass flow rates, while at lower mass flow rates the curve shows a flatter trajectory. At a mass flow rate of 6 kg/h, an optimum d_{hyd} of 2.6 mm becomes apparent. This means that the design of the optimum hydraulic diameter becomes increasingly important at higher mass flow rates. The results demonstrate a positive correlation between mass flow rate and CHF. This can be attributed to enhanced heat transfer due to increased turbulence and boundary layer thinning at higher flow rates. As the flow rate increases, the fluid can absorb more heat before reaching the critical point where film boiling occurs. An interesting observation is the existence of an optimal channel diameter for maximizing CHF at high flow rates. This behavior can be explained by considering the balance between two competing factors: surface area and pressure drop. Smaller channels offer a larger heat transfer surface area but also experience higher pressure drop. Conversely, larger channels have lower pressure drop but less surface area. The optimal diameter strikes a balance between these factors for efficient heat transfer at high flow rates.

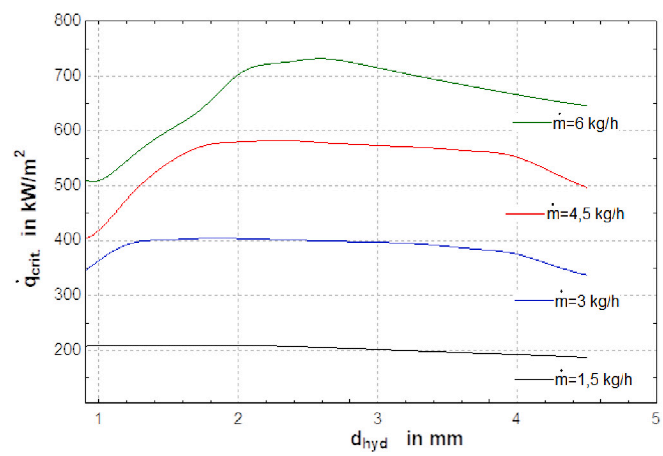

Fig. 15. Influence of d_{hyd} on CHF.

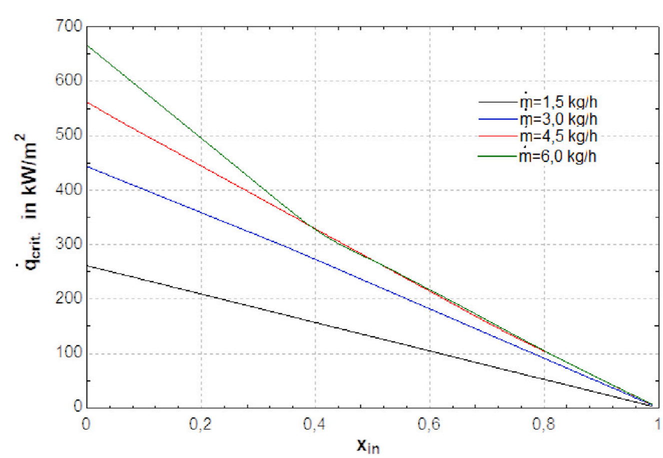

Fig. 16. Influence of inlet vapor content on CHF.

Within the myriad of geometrical parameters, both the hydraulic diameter and the length/diameter ratio have a significant influence on the CHF. In the context of subcooled boiling, the CHF shows an increase with decreasing channel diameter, a trend consistently observed by several researchers [28,29]. Conversely, for $x_{in} > 0$ the CHF also decreases with decreasing diameter. Bergles [29] hypothesized that a reduction in channel diameter leads to a concomitant reduction in the exit diameter of vapor bubbles. In addition, condensation at the bubble tip increases and the velocity of the bubble relative to the liquid decreases. These combined effects contribute to the curve shown in Fig. 15.

7.2. Effect of inlet vapor quality on CHF

The influence of inlet vapor quality, denoted by x_{in}, on the CHF exhibits a well-defined trend, as illustrated in Fig. 16. This trend can be analyzed through the lens of the liquid film thickness on the heated surface. As the inlet vapor quality increases, the mass flow rate of the liquid phase at the inlet decreases. Consequently, the liquid film on the heated surface thins. This thinning film plays a crucial role in heat transfer. A thicker liquid film facilitates more efficient heat transfer from the heated surface to the bulk liquid. Conversely, a thinner film impedes heat transfer, leading to a rise in surface temperature.

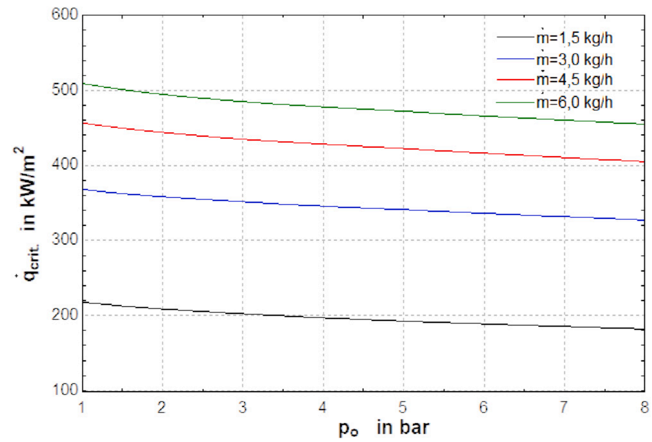

Fig. 17. Influence of the evaporation pressure on CHF.

Following the logic established in [30,31], CHF is reached when the liquid film thickness on the heated surface reaches a minimum critical value. Beyond this point, the film becomes too thin to effectively transfer heat, and a vapor blanket forms on the surface. This vapor blanket significantly reduces heat transfer, leading to a rapid rise in surface temperature. This phenomenon explains the observed decrease in CHF with increasing inlet vapor quality. As the liquid mass flow rate diminishes with higher vapor quality, the critical film thickness is reached at a lower overall heat flux, resulting in a lower CHF value.

7.3. Role of evaporation pressure in CHF dynamics

The effect of evaporation pressure on CHF is shown in Fig. 17. The trend indicates that as the evaporation pressure escalates, the CHF achievable in the SHME decreases. This behavior results from the interaction of two opposing effects. On the one hand, the increase in pressure increases the CHF [12]. On the other hand, it simultaneously decreases the enthalpy of evaporation. Since the decrease in the enthalpy of evaporation outweighs the increase in the CHF, a lower power input is sufficient to reach the critical vapor content. This phenomenon is consistent with the observations of Mauro et al. [24].

8. Conclusions

This study conducted a comprehensive investigation into the influence of several key variables on the CHF in a SHME with a specific design. The SHME employed in this study featured a single helical coil with rectangular channels, fin thickness of 0.6 mm and hydraulical diameters from 0.84 mm to 3.7 mm. A designated area with a 6 mm pitch swirl-generating insert was used as a representative case, with the same analytical approach applied to all measurements. This analysis focused mainly on the evaporation pressure p_o, condensation pressure p_c, mass flow $\dot{m}$, electrical power $\dot{Q}_{el}$ and the temperatures of the thermocouples T_1–T_5 in the refrigerated element.

The analysis of the experimental data revealed that a higher mass flow rate resulted in a significant increase in CHF. This can be attributed to the enhanced ability of the liquid phase to absorb heat and replenish the liquid film on the heated surface, improving heat transfer efficiency. Experimental data also indicated a complex relationship between channel hydraulic diameter and CHF. Smaller channel hydraulic diameters generally exhibited a higher CHF due to the increased surface area for heat transfer. However, smaller channels are also more susceptible to flow instabilities and pressure drops, which can negatively impact CHF at high flow rates.

This study focused on specific experimental parameters (hydraulic diameters, mass flux), and fixed test specimen geometry (bore diameter and depth). While valuable, this approach limited the scope of the investigation. To overcome these limitations and gain broader insights, one computational model has been developed and validated. By utilizing experimental data for validation, a wider range of operating conditions were explored beyond the capabilities of the test stand. This computational approach allowed us to investigate the influence of various parameters on CHF in SHMEs and achieve high prediction accuracy. While our current study had a specific dataset size (32 measurements), future work will aim to expand the experimental data range to enhance the generalizability of the model.

Conclusions are primarily applicable to the specific SHME design and operating conditions investigated in this study. However, the observed trends provide valuable insights into the factors affecting CHF in SHMEs. Future research can expand on this work by investigating a wider range of SHME geometries, materials, and operating parameters to establish more generalizable design guidelines and optimize SHME performance for various applications.

The systematic comparison of experimental and simulated data provided valuable insights into the operating characteristics of the system. The transition from the nucleate boiling range to the point where the CHF was exceeded resulted in an abrupt increase in temperature, an important observation for predicting and managing system behavior.

A key achievement of this research was the application and refinement of the Groeneveld method to accurately predict the CHF point. This method offers critical advantages in ensuring operational safety and achieving high efficiencies, as the heat transfer coefficient peaks near the CHF point. Strong correlation was observed between the experimental results and the prediction of the CHF by this model, allowing its validation and further extrapolation to conditions beyond the capacities of the experimental setup. Furthermore, the influence of several parameters on the CHF was studied in detail, including the hydraulic diameter, the inlet vapor quality and the evaporation pressure.

This extrapolation allows to conclude that as the inlet vapor quality increases, the CHF exhibits a decreasing trend. This is because a higher vapor quality signifies a lower mass flow rate of the liquid phase at the inlet. Consequently, the liquid film on the heated surface thins, leading to a deterioration in heat transfer capability and a lower CHF value. It was also concluded that at high flow rates there exists an optimal hydraulic diameter that maximizes CHF. The decrease in CHF with increasing evaporation pressure was also confirmed.

This study offers valuable contributions to the field of boiling heat transfer. New physical insights are revealed regarding the influence of helical channels on CHF. The validated model captures these mechanisms, leading to a more comprehensive understanding of boiling in this specific configuration. Furthermore, the model's framework has the potential to be adapted for other microchannel designs with helical features, suggesting broader applicability.

In conclusion, this work has significantly advanced the understanding of the behavior of SHMEs under different conditions, particularly in relation to CHF. Accurate CHF estimation is critical for the safe and efficient operation of SHMEs in various applications, such as hot spot cooling in injection molding, special-purpose machinery applications like Sonotrode cooling and power electronics cooling systems, among others. By understanding how factors like mass flow rate and hydraulic diameter influence CHF, engineers can design and operate SHMEs to avoid exceeding their limits, preventing overheating and potential system failure. The agreement between the experimental results and the simulation results provides confidence in the developed model. These results, coupled with the extrapolations of the model, will serve as a robust basis for future research in this area. It is expected that the knowledge gained from this study will significantly contribute to the optimization of the design and operation of thermal systems, thus promoting progress towards safer and more efficient thermal applications.

CRediT authorship contribution statement

M. Feiner: Writing – original draft, Validation, Software, Investigation. **F.J. Fernández:** Supervision, Methodology, Formal analysis. **M. Arnemann:** Methodology, Conceptualization. **M. Kipfmüller:** Supervision, Resources, Project administration, Funding acquisition.

Declaration of competing interest

The authors declare the following financial interests/personal relationships which may be considered as potential competing interests: Matthias Feiner reports financial support was provided by German Federal Ministry for Economic Affairs and Climate Action.

Data availability

A Mendeley dataset titled 'Experimental Data on Critical Heat Flux of Short Helical Minichannel Evaporators' has been created.

Acknowledgments

This document is the result of the research project 'Cool Tool' ZF4102824TV8 funded by the German Federal Ministry for Economic Affairs and Climate Action.

References

[1] M. Stein, Systematische Untersuchung der kritischen Wärmestromdichte beim Strömungssieden von Wasser in lotrechten Kreisrohren mit und ohne poröser Beschichtung (Ph.D. thesis), Technische Universität Berlin, Fakultät III - Prozesswissenschaften, 2004.
[2] B. Agostini, M. Fabbri, J.E. Park, L. Wojtan, J.R. Thome, B. Michel, State of the art of high heat flux cooling technologies, Heat Transf. Eng. 28 (4) (2007) 258–281.
[3] S. Abishek, R. Narayanaswamy, V. Narayanan, Effect of heater size and Reynolds number on the partitioning of surface heat flux in subcooled jet impingement boiling, Int. J. Heat Mass Transfer 59 (2013) 247–261.
[4] M. Manno, B. Yang, S. Khanna, P. McCluskey, A. Bar-Cohen, Microcontact-enhanced thermoelectric cooling of ultrahigh heat flux hotspots, IEEE Trans. Compon., Packag. Manuf. Technol. 5 (12) (2015) 1775–1783.
[5] S.K. Saha, G.P. Celata, Microchannel Phase Change Transport Phenomena, Elsevier, 2016.
[6] M. Feiner, M. Arnemann, M. Kipfmüller, Development of an adjustable spiral-shaped evaporator, in: Proceedings of the 17th International Refrigeration and Air Conditioning Conference, 9.-12. July 2018, Purdue University, West Lafayette, Indiana, USA, 2018.
[7] M. Feiner, F.J. Fernández García, M. Arnemann, M. Kipfmüller, Hydraulic characterization of a adjustable spiral-shaped evaporator, in: Proceedings of the 18th International Refrigeration and Air Conditioning Conference, 23.-27. May 2021, Purdue University, West Lafayette, Indiana, USA, 2021.
[8] A.M. Elsayed, Heat Transfer in Helically Coiled Small Diameter Tubes for Miniature Cooling Systems (Ph.D. thesis), University of Birmingham, 2011.
[9] J.-W. Kim, Y.-B. Im, J.-S. Kim, A study on performance analysis of the helically coiled evaporator with circular minichannels, J. Mech. Sci. Technol. 20 (7) (2006) 1059–1067.
[10] J.-W. Kim, J.-H. Kim, J.-S. Kim, A study on the helically coiled heat exchanger of small diameter tubes, Trans. Korean Soc. Mech. Eng. B 25 (11) (2001) 1492–1499.
[11] J.-W. Kim, J.-H. Kim, S.-K. Seo, J.-H. Kim, J.-S. Kim, Characteristics of heat transfer and pressure drop of R-22 inside an evaporating tube with small diameter helical coil, Trans. Korean Soc. Mech. Eng. B 24 (5) (2000) 699–708.
[12] D.C. Groeneveld, J.Q. Shan, A.Z. Vasić, L. Leung, A. Durmayaz, J. Yang, S.C. Cheng, A. Tanase, The 2006 CHF look-up table, Nucl. Eng. Des. 237 (15–17) (2007) 1909–1922.
[13] B. Hardik, S. Prabhu, Experimental correlation for critical heat flux in helical coils, Nucl. Eng. Des. 368 (2020).
[14] T. Knipping, Kühlen kleiner Kavitäten mit verdampfenden Fluiden, DKV Deutscher Kälte-und Klimatechnischer Verein e.V., Forschungsbericht Nr. 88, 2018.
[15] W. Bohl, Strömungsmaschinen - Aufbau und Wirkungsweise, Vogel, Würzburg, 2008.
[16] D. Groeneveld, J. Shan, A. Vasić, L. Leung, A. Durmayaz, J. Yang, S. Cheng, A. Tanase, The 2006 CHF look-up table, Nucl. Eng. Des. 237 (15–17) (2007) 1909–1922.
[17] D. Groeneveld, A. Ireland, J. Kaizer, A. Vasic, An overview of measurements, data compilations and prediction methods for the critical heat flux in water-cooled tubes, Nucl. Eng. Des. 331 (2018) 211–221.
[18] N.I. Kolev, Check of the 2005-look up table for prediction of CHF in bundles, Nucl. Eng. Des. 237 (9) (2007) 978–981.
[19] W.-P. Baek, H.-C. Kim, S.H. Chang, An independent assessment of groeneveld et al.'s 1995 CHF look-up table, Nucl. Eng. Des. 178 (3) (1997) 331–337.
[20] J.H. Song, J. Lee, S.H. Chang, Y.H. Jeong, Correction factor development for the 2006 groeneveld CHF look-up table for rectangular channels under low pressure, Nucl. Eng. Des. 370 (2020) 110869.
[21] I. Pioro, D. Groeneveld, S. Cheng, S. Doerffer, A. Vasić, Y.V. Antoshko, Comparison of CHF measurements in R-134a cooled tubes and the water CHF look-up table, Int. J. Heat Mass Transfer 44 (1) (2001) 73–88.
[22] DIN 1319-1:1995-01, Grundlagen der Meßtechnik_- Teil_1: Grundbegriffe, Beuth Verlag GmbH, Berlin, 1995.
[23] H.-R. Tränkler, G. Fischerauer (Eds.), Das Ingenieurwissen: Messtechnik, Springer, Berlin, Heidelberg, 2014.
[24] A. Mauro, J. Thome, D. Toto, G.P. Vanoli, Saturated critical heat flux in a multi-microchannel heat sink fed by a split flow system, Exp. Therm Fluid Sci. 34 (1) (2010) 81–92.
[25] A. Roday, M. Jensen, Study of the critical heat flux condition with water and R-123 during flow boiling in microtubes. Part I: Experimental results and discussion of parametric effects, Int. J. Heat Mass Transfer 52 (13–14) (2009) 3235–3249.
[26] A. Roday, M. Jensen, Study of the critical heat flux condition with water and R-123 during flow boiling in microtubes. Part II–comparison of data with correlations and establishment of a new subcooled CHF correlation, Int. J. Heat Mass Transfer 52 (13–14) (2009) 3250–3256.
[27] B. Agostini, R. Revellin, J.R. Thome, M. Fabbri, B. Michel, D. Calmi, U. Kloter, High heat flux flow boiling in silicon multi-microchannels–Part III: Saturated critical heat flux of R-236fa and two-phase pressure drops, Int. J. Heat Mass Transfer 51 (21–22) (2008) 5426–5442.
[28] C. Vandervort, A. Bergles, M. Jensen, An experimental study of critical heat flux in very high heat flux subcooled boiling, Int. J. Heat Mass Transfer 37 (1994) 161–173.
[29] A.E. Bergles, Forced-Convection Surface-Boiling Heat Transfer and Burnout in Tubes of Small Diameter (Ph.D. thesis), Massachusetts Institute of Technology, 1962.
[30] G. Hetsroni, A. Mosyak, E. Pogrebnyak, Z. Segal, Periodic boiling in parallel micro-channels at low vapor quality, Int. J. Multiph. Flow 32 (10–11) (2006) 1141–1159.
[31] J. Lee, I. Mudawar, Two-phase flow in high-heat-flux micro-channel heat sink for refrigeration cooling applications: Part II— heat transfer characteristics, Int. J. Heat Mass Transfer 48 (5) (2005) 941–955.